Advanced Integrated Power Centre with Electric Power Transfer Capability

Serhiy Bozhko, Patrick Wheeler
Power Electronics, Machines and Control Group
The University of Nottingham
UNITED KINGDOM

serhiy.bozhko@nottingham.ac.uk, pat.wheeler@nottingham.ac.uk

Keywords: Workshop, More-Electric Aircraft, Electric Power Transfer, Back-to-Back Converter, Engine Performance

ABSTRACT

This paper proposes an advanced integrated power generation centre for future more electric aircraft. To fully exploit the power supply ability of the twin-spool engine, a dual-generator configuration is applied, where a starter/generator is coupled to the high-pressure shaft, and a generator is coupled to the low-pressure shaft. They are independently controlled by two active rectifiers. The DC sides of these are connected in a parallel, supplying power to a common DC bus. The key novelty is introduction of a back-to-back converter to bridge the AC terminals of the two generators. A variety of enhanced functions can be achieved by this innovative configuration, including efficient electric power transfer between engine spools, power decoupling between the engine and the DC grid, removal of flux weakening operation of high-pressure spool generator at high speed, post-fault operation, etc. The paper presents the control design for such a power-electronic based system and illustrates the benefits of proposed power offtake arrangements.

1.0 INTRODUCTION

During the past decades, aiming for improved environmental impact, a great progress has been made towards development of more-electric aircraft (MEA) and more-electric engine (MEE) due to advantages of their higher efficiency, decreased fuel consumption, and lower maintenance costs (Wheeler et al., 2013, [1]). As many onboard components and systems which consume hydraulic or pneumatic energies are replaced by their electrically powered counterparts, there is a substantial increase of onboard electric power demand. Since the prime energy source is the engine, establishing the ways of optimal power offtake and power conversion arrangements are of great importance. For a twin-spool MEE, an effective solution for coordinated mechanical power offtake from both low-pressure (LP) and high-pressure (HP) shafts using two separated electric machines (generators) coupled to the two MEE spools is proposed in (Enalou and Bozhko, 2020, [6]). However, when significant power offtake from MEE is required, this should be arranged such that the constraints imposed by the engine structure are met. In a traditional turbofan engine, there is no physical connection between LP and HP spools, however, they are coupled thermodynamically. Thus, their performance in terms of compressor surge margin or efficiency cannot be optimized for the entire range of engine operation modes (Enalou and Bozhko, 2020, [6]).

The increased onboard electric power demand in MEA also results in significant evolution of onboard electric power systems (EPS) with new topology paradigms considered to achieve the most efficient distribution of electric power to the loads. One of such concepts, known as single-bus topology (Gao and Bozhko, 2016, [3]), assumes multiple sources running in parallel to optimise load power sharing in the most efficient way, hence minimizing weight and maximizing efficiency of the electric power generation system onboard. In the meantime, this approach in electrical domain offers a unique opportunity to influence thermodynamic one, in order to maximize benefits for future aircraft platform. This is the key target of this study that introduces an Advanced Integrated Power Centre (AIPC).

To achieve full exploitation of the MEE power supply ability, the power offtake from the two shafts is proposed to be arranged in a coordinated way (Enalou and Bozhko, 2020, [6]). By specific control of electric machines, which are naturally bidirectional, AIPC establishes a decoupled operation of the LP and HP spools. The configuration of proposed AIPC is illustrated by in Figure 1. Here, two electrical generators (denoted as LPG and HPG) are driven by different engine spools. The generators are independently controlled by dedicated rectifiers and supply a common DC bus running in parallel. Different onboard power loads are fed from this bus. As one can see, such configuration can offer a channel for electrical power exchange between the electric machines through the common DC bus, hence between the MEE shafts. It means there is a route for power exchange between the shafts which can be exploited as a tool to establish the desirable shaft decoupling. However, in this study goes further and introduces an advanced topology with additional back-to-back (BTB) power electronic converter, which is specifically deployed as a AC/AC power bridge connecting the AC terminals of two electrical generators.

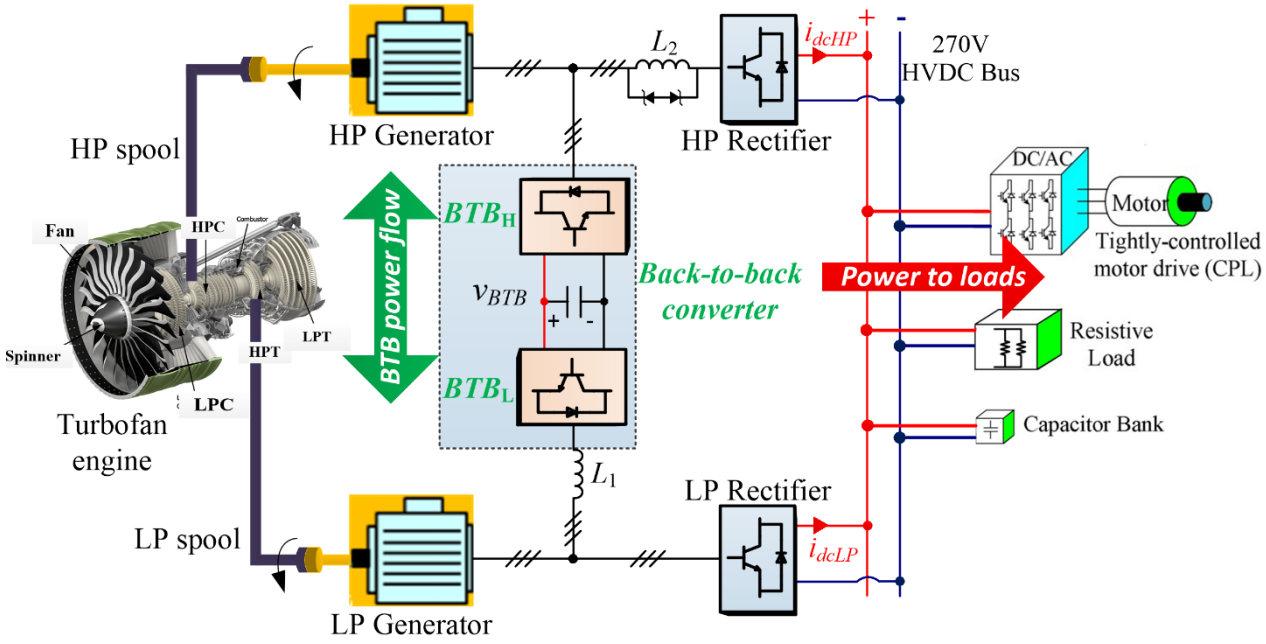

Figure 1. The proposed AIPC with a back-to-back converter.

A variety of benefits can be delivered by this novel structure, including:

1) Electric power transfer (EPT): the BTB converter can perform as a bidirectional power bridge, allowing power transfer from the LP to HP channel, or vice versa. In this way, one of the generators can operate in motoring mode, transferring mechanical power to the coupled engine spool. Through this feature, the MEE can be operated in the way which is the most optimised for various flight scenarios - in terms of fuel consumption, efficiency, engine stability, and compatible thrust with flight mission;

2) Removal of field-weakening operation: in the high-speed setting mode such as cruise, HP spool is operated at a high speed. As reported in (Li et al., 2019, [7]), the HP speed can be as high as 20,000 rpm. Considering the potential high back EMF due to a high rotary speed and limited DC bus voltage, field-weakening control is required to guarantee the safe operation of HP generator. Considerable de-fluxing current will circulate, causing significant power loss. In the proposed AIPC, the BTB converter can be designed with a high internal DC-link voltage, thus eliminating the need of field-weakening operation. Therefore, copper loss of generator and conduction loss of converter are significantly reduced, further improving efficiency of the entire system;

3) Fault tolerance improvement: if any fault occurs to the HP or LP rectifiers, the faulty rectifier can be stopped and disconnected from the AIPC. In this case, the BTB converter can still provide a path for power flow, allowing the two generators to supply interrupted power to the onboard loads on the main DC bus.

As can be seen in Figure 1, since multiple generators and power converters are integrated in the AIPC, coordinated control design and power management are of great importance. A turbofan engine model implemented in a dSpace platform is considered as part of the AIPC, thus the physical variables such as shaft speed and torque can be fed to the engine model in real time. This configuration allows to study the benefits of EPT on engine.

The rest of this paper is organized as follows. In Section 2, the control plant analysis and control design for the main AC/DC rectifiers are illustrated, aiming to provide a robust control of the main DC bus voltage and achieve power sharing between the two rectifiers. The power transfer management strategy for the BTB converter is presented in Section 3, where a phase current synchronization method is proposed to fulfil this goal. Experimental results are presented in Section 4, verifying the control performance of the AIPC and the improvement of engine's compressor surge margin. Section 5 concludes this paper.

2.0 DC BUS VOLTAGE CONTROL FOR MAIN RECTIFIERS

2.1 Analysis of Control Plant

Since there are two main AC/DC rectifiers (denoted as LPR and HPR) supplying power to the DC bus, appropriate power sharing between them is required. A current-mode droop control method presented in (Li et al., 2019, [7]) is adopted due to advantages including the absence of communication link, high modularity, and immunity from the impact of cable impedance. The power sharing is achieved by splitting the total load current i_{dc} into currents i_{dcLP} and i_{dcHP}. Using droop control characteristic, the DC current reference can be derived as shown in Equation (1):

$$i_{dc}^{*} = \frac{v_{dc}^{*} - v_{dc}}{g_D} \tag{1}$$

where g_D is the droop gain, v_{dc} is the DC-bus voltage, and v_{dc}^{*} - the DC-bus voltage reference. With the current-mode droop control, the output of control plant should be the DC current i_{dc} to regulate DC voltage changes caused by the load currents. The DC link equation can be formulated as given in Equation (2):

$$C\frac{dv_{dc}}{dt} = i_{dc} - i_L \tag{2}$$

where C is the capacitance of main DC bus capacitor, i_L is the load current.

Permanent magnet machine (PMM) based generators are considered for both HP and LP channels due to their advantages in power density, wide speed range and high efficiency. The electrical dynamics of PMM in the *dq* rotary frame can be given as shown in Equation (3):

$$\begin{cases} \dfrac{di_d}{dt} = \dfrac{1}{L_d}\left(v_d - R_s i_d + \omega_e L_q i_q\right) \\ \dfrac{di_q}{dt} = \dfrac{1}{L_q}\left(v_q - R_s i_q - \omega_e L_d i_d - \omega_e \psi_m\right) \end{cases} \tag{3}$$

where v_d and v_q are stator voltages in d and q axes, respectively; i_d and i_q are stator currents in d and q axes,

respectively; L_d and L_q are stator inductance; R_s is the stator resistance; ψ_m is the flux linkage of permanent magnet; ω_e is the electrical speed in rad/s. For surface-mounted PMM, $L_d = L_q = L_s$.

Based on the assumption of a negligible power losses on rectifier, the power balance equation of the rectifier can be expressed as follows:

$$1.5\left(v_d i_d + v_q i_q\right) = v_{dc} i_{dc} \tag{4}$$

The control plant for i_{dc} control can be derived from the DC link dynamics shown in Equation (2), the PMM electrical dynamics in Equation (3), and the power balance relation in Equation (4). With small signal analysis, it can be given as follows:

$$\left[\frac{2\bar{v}_{dc}{}^2 Cs - 3\left(\bar{v}_d \bar{i}_d + \bar{v}_q \bar{i}_q\right)}{2\bar{v}_{dc} Cs}\right]\Delta i_{dc} = \frac{3}{2}\begin{Bmatrix} -\left[\bar{v}_d \Delta i_d + \bar{i}_d \begin{pmatrix} (R_s + L_s s)\Delta i_d \\ -\omega_e L_s \Delta i_q \end{pmatrix}\right] \\ -\left[\bar{v}_q \Delta i_q + \bar{i}_q \begin{pmatrix} (R_s + L_s s)\Delta i_q \\ +\omega_e L_s \Delta i_d \end{pmatrix}\right] \end{Bmatrix} \tag{5}$$

where the overbar indicates the selected operating points. The relation shown in Equation (5) can be rearranged as follows:

$$\Delta i_{dc} = \frac{3\bar{v}_{dc} Cs}{2\bar{v}_{dc}{}^2 Cs - 3\left(\bar{v}_d \bar{i}_d + \bar{v}_q \bar{i}_q\right)}\begin{Bmatrix} -\left[\bar{v}_d + \omega_e L_s \bar{i}_q + \left(R_s + L_s s\right)\bar{i}_d\right]\Delta i_d \\ -\left[\bar{v}_q - \omega_e L_s \bar{i}_d + \left(R_s + L_s s\right)\bar{i}_q\right]\Delta i_q \end{Bmatrix} \tag{6}$$

Based on Equation (6), and consider the current loop dynamic as a second-order transfer function, the control plant can be derived as shown in Figure 2, where the expression of f_d and f_q are given in Equation (7):

$$\begin{cases} f_d = -\dfrac{\omega_c{}^2}{s^2 + 2\zeta\omega_c s + \omega_c{}^2}\dfrac{3\bar{v}_{dc} Cs\left[\bar{v}_d + \omega_e L_s \bar{i}_q + \left(R_s + L_s s\right)\bar{i}_d\right]}{2\bar{v}_{dc}{}^2 Cs - 3\left(\bar{v}_d \bar{i}_d + \bar{v}_q \bar{i}_q\right)} \\ f_q = -\dfrac{\omega_c{}^2}{s^2 + 2\zeta\omega_c s + \omega_c{}^2}\dfrac{3\bar{v}_{dc} Cs\left[\bar{v}_q - \omega_e L_s \bar{i}_d + \left(R_s + L_s s\right)\bar{i}_q\right]}{2\bar{v}_{dc}{}^2 Cs - 3\left(\bar{v}_d \bar{i}_d + \bar{v}_q \bar{i}_q\right)} \end{cases} \tag{7}$$

where ζ and ω_c are damping ratio and natural frequency, respectively, of the inner current loop.

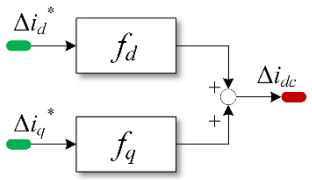

Figure 2. Control plant for the i_{dc} control system.

To study the stability of control plant at different operating points, the closed loop response of the plant using a proportional controller was investigated. The proportional gain is denoted as K_{vP}. Figure 3 and Figure 4 show the closed loop root locus at different speeds of generator and different load powers. It can be seen that the closed loop poles move towards the right half plane (RHP) as the increase of K_{vP}. The value of K_{vP} must be carefully selected to ensure that the poles do not move cross the imaginary axis into the RHP, otherwise the system will become unstable.

It can be seen from Figure 3 that as the speed increases, the allowed value for K_{vP} decreases from 1.14 to 0.59. Also, from Figure 4, one can see that as the load power increases, the allowed value for K_{vP} decreases from 0.85 to 0.66. These results show that the worst operating point corresponds to the highest speed and full power. Hence, this operating point is specifically considered when designing the i_{dc} proportional-integral controller.

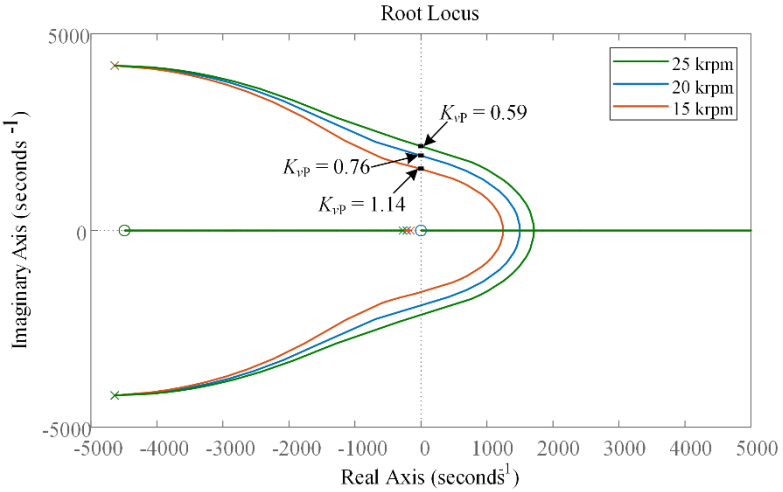

Figure 3. Closed loop root locus of control plant at different speeds. Load power is 15kW.

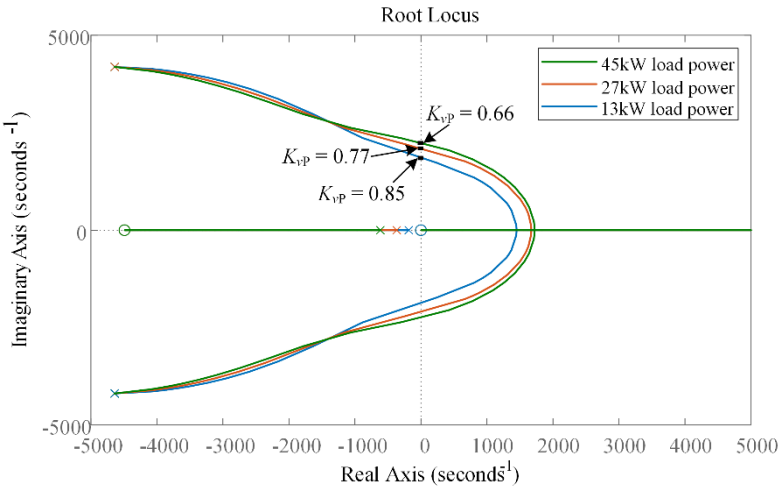

Figure 4. Closed loop root locus of control plant at different load powers. Operating speed is 20 krpm.

2.2 DC Bus Voltage Control Design

In the proposed AIPC, the DC-link voltage of the BTB converter can be set to a high value, ensuring the HP generator can operate without field-weakening. Thus, i_d can be controlled to zero for the surface-mounted PMM in use. Hence, a reasonable assumption was made for the following control design, which is that the influence of i_d is neglected. The dynamics of Δi_{dc} are dominated by Δi_q. With this assumption, the block diagram of the DC bus voltage control can be derived as shown in Figure 5.

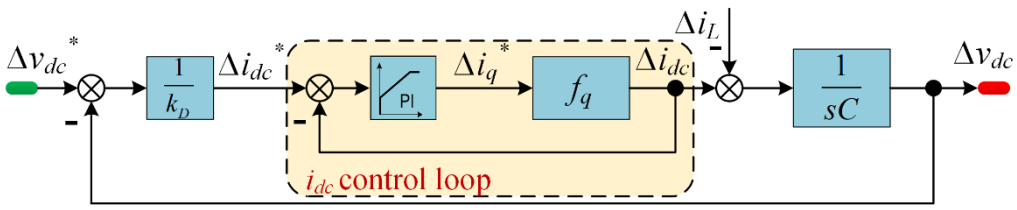

Figure 5. Block diagram of the DC bus voltage control.

As shown in Figure 5, a proportional-integral (PI) controller is applied to regulate the inner i_{dc} control loop. The controller can be expressed as shown in Equation (8):

$$G_{pi}(s) = K_{vP} + \frac{K_{vI}}{s} \tag{8}$$

With the f_q in Equation (5) and consider Equation (6), the open loop transfer function of the i_{dc} control loop can be derived as Equation (9) shows::

$$G_{op}(s) = -\frac{\left(K_{vP}s + K_{vI}\right)\omega_c^2}{s^2 + 2\zeta\omega_c s + \omega_c^2} \frac{3\bar{v}_{dc}C\left[\bar{v}_q - \omega_e L_s \bar{i}_d + \left(R_s + L_s s\right)\bar{i}_q\right]}{2\bar{v}_{dc}^2 Cs - 3\left(\bar{v}_d\bar{i}_d + \bar{v}_q\bar{i}_q\right)} \tag{9}$$

As can be seen in (8), there are three poles in $G_{op}(s)$, and two out of the three are conjugate poles brought by the current loop transfer function. To study the effect of the three poles, their locations on the complex plane are plotted with respect to different speeds and load power, as shown in Figure 6. It can be seen that the location of the two conjugate poles is fixed because ζ and ω_c only depend on the current-loop control parameters and generator parameters (Lang et al., 2019, [11]). The dominant pole depends on the operating point. With the increase of speed and load power, it moves toward the RHP, indicating a degraded stability.

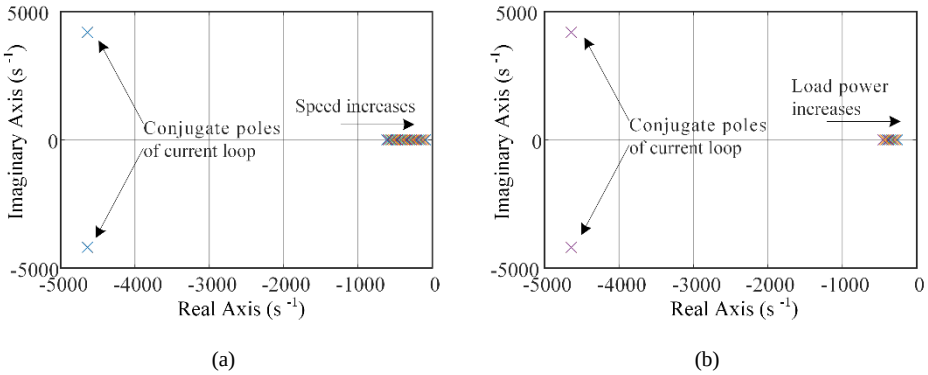

Figure 6. Locations of $G_{op}(s)$ poles at different speeds and load powers.

The i_{dc} PI controller provides a zero. To cancel the dominant pole with this zero, the control parameters can be set as shown in Equation (10):

$$\begin{cases} K_{vP} = 2\bar{v}_{dc}^2 C \cdot \gamma \\ K_{vI} = -3\left(\bar{v}_d\bar{i}_d + \bar{v}_q\bar{i}_q\right) \cdot \gamma \end{cases} \tag{10}$$

where γ is a gain used to tune the control parameters. From (10) it can be seen that the PI parameters depend

on operating points and on gain γ. By applying Equation (10) into Equation (8), the open loop transfer function of the i_{dc} control loop can be derived as shown in Equation (11):

$$G_{op}(s) = -\frac{3\gamma \bar{v}_{dc} C\omega_c^2 \left[\bar{v}_q - \omega_e L_s \bar{i}_d + (R_s + L_s s)\bar{i}_q\right]}{s^2 + 2\zeta\omega_c s + \omega_c^2} \tag{11}$$

As concluded above, the higher speed and heavier load power are identified as the worst operating conditions in terms of control stability. The root locus of $G_{op}(s)$ is analysed at the point (32k rpm, 45kW) and shown in Figure 7. The trajectory means the locations of closed loop poles at different values of the gain γ. It can be seen when γ is set as 0.4, the damping ratio is 0.707 and the overshoot is 3.9%. This is an acceptable performance in the worst operating condition. Hence, the gain γ is set as 0.4 in the following analysis. With the known value of γ, the control parameters can be adaptively tuned based on the relation in Equation (10).

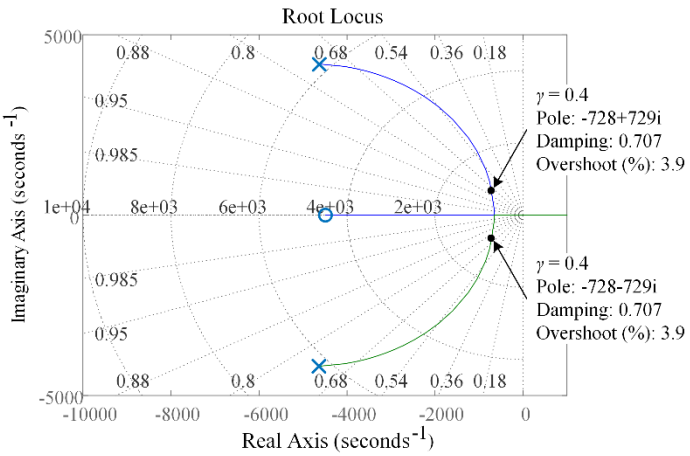

Figure 7. Root locus of $G_{op}(s)$ at 32 krpm, 45kW.

To conclude above, the control block diagram can be built as shown in Figure 8, where the design criteria of control parameters are highlighted.

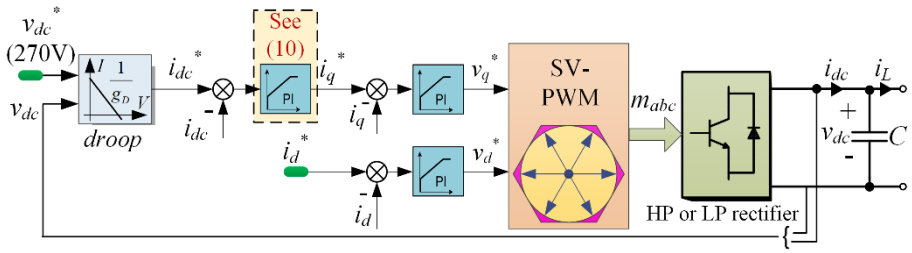

Figure 8. Control block diagram for the HP and LP rectifiers.

3.0 PHASE CURRENT SYNCHRONIZATION CONTROL FOR THE BACK-TO-BACK CONVERTER

As shown in Figure 1, the BTB converter consists of two separate AC/DC converters, denoted as BTB_L converter and BTB_H converter, respectively. For the BTB_L converter, since AC terminals of the LP generator and BTB_L converter share the same junctions *a*, *b*, and *c* as shown in Figure 9, an effective way to control the transferred power from the LP channel to the BTB converter is to control the phase currents of LPG (i_{xLP})

and BTB_L converter (i_{xBTBL}, x=a,b,c) (as shown in Figure 9) in phase. If i_{xLP} and i_{xBTBL} can be synchronized, i.e., controlled in phase, by manipulating the ratio of magnitude of AC currents i_{xLP} and i_{xBTBL}, the power transferred to/from the BTB converter can be controlled.

Apart from regulating currents in phase, the control scheme for the BTB_L converter is also responsible for the BTB converter DC-link voltage (v_{BTB}) control. However, in the conventional control schemes for applications such as active front end (AFE) (Jalili and Bernet, 2009, [9]) or flywheel energy storage system [10], the output of outer voltage controller is the reference of active power or active current. This structure will not be able to control i_{xBTBL} and i_{xLP} in phase. To address this issue, a new method is proposed to realize the following two functions:

1) BTB converter DC-link voltage (v_{BTB}) regulation.
2) In-phase control of phase currents i_{xBTBL} and i_{xLP} (x=a,b,c).

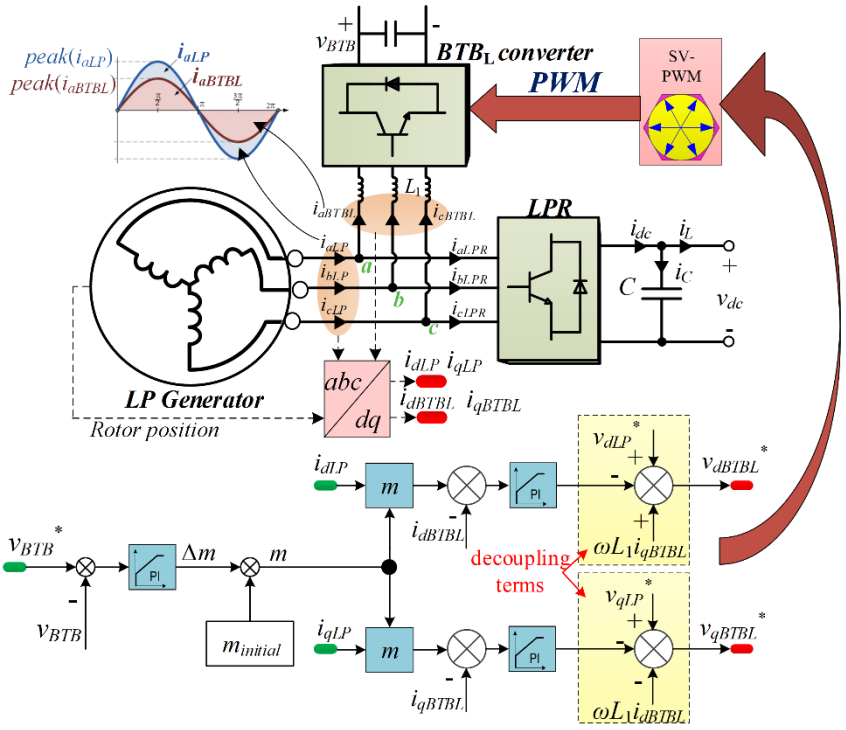

Figure 9. The control schematic for the BTB_L converter.

As can be seen from Figure 9, in contrast to the control schemes (Jalili and Bernet, 2009, [9]), (Zhang and Yang, 2017, [10]), where the output of voltage controller is active current or power reference, in the proposed structure, both *dq* axes current references are the sensed LPG's *dq* axes currents multiplied by a gain *m*. If the phase currents i_{xBTBL} and i_{xLP} are processed by the same *abc/dq* transformation related to the LPG rotor position in the studies case, it is expected that i_{xBTBL} and i_{xLP} will be synchronized in phase, and the gain *m* defines their magnitude ratio (i_{xBTB1} over i_{xLP}).

Based on the synchronized phase currents i_{xBTBL} and i_{xLP}, the gain *m* is used to regulate the DC voltage v_{BTB}. If v_{BTB} drops below its reference, *m* will be increased by the control action so that more power will be transferred to the BTB converter to charge the internal DC-link capacitor, increasing v_{BTB}, and vice versa. Therefore, with the proposed control strategy, v_{BTB} can be stabilized and i_{xBTBL} and i_{xLP} can be synchronized. In the steady state, the power generated by LPG P_{LPG} and the power transferred to the BTB converter P_{BTB} have

the following relationship:

$$\frac{peak(i_{aLP})}{peak(i_{aBTBL})} = \frac{i_{qLP}}{i_{qBTBL}} = \frac{i_{dLP}}{i_{dBTBL}} = \frac{P_{LP}}{P_{BTB}} = \frac{1}{m} \tag{12}$$

To conclude, the main difference of the proposed control scheme in Figure 9 and the conventional control schemes is how to acquire current reference, specifically:

- In the conventional control schemes, active current reference directly comes from the output of voltage controller.
- In the proposed control scheme, current references are measured dq axes currents of LPG multiplied by the factor m defined by Equation (12). The value of m is defined by the outer voltage loop to stabilize the DC-link voltage of the BTB converter.

The proposed phase current synchronization method and BTB converter DC voltage control method is further analysed in the following subsections to ensure stability and control performance.

3.1 Current-Loop Bandwidth for the BTB_L Converter

As shown in Figure 9, the current references are measured *dq* axes currents of LPG multiplied by the factor m. Hence, when selecting the current-loop bandwidth for the BTB_L converter, the bandwidth of LPG's stator current control loop should be considered. A *q*-axis current step response test is carried out as shown in Figure 10, where the LPG's stator current loop bandwidth is selected as 1kHz for the given high speed drive system (Bozhko et al., 2017, [12]), and the current-loop bandwidth for the BTB_L converter is 700Hz, 1kHz and 1.5kHz, respectively.

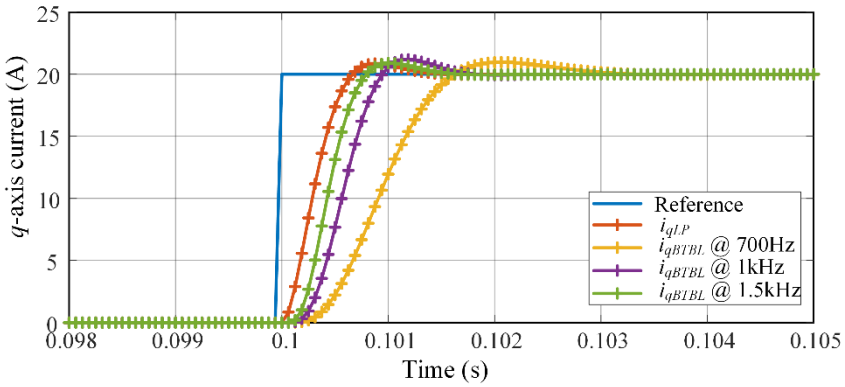

Figure 10. Step response test of i_q with different current-loop bandwidth for the BTB_L converter.

In Figure 10. Step response test of i_q with different current-loop bandwidth for the BTB_L converter., the reference for *q*-axis current of LPG (i_{qLP}) steps to 20A at 0.1s. The response can be observed in the red curve. i_{qLP} response serves as *q*-axis current reference for the BTB_L converter. It can be seen that as the increase of bandwidth for the BTB_L converter, the *q*-axis current of the BTB_L converter (i_{qBTBL}) tracks i_{qLP} with faster dynamics. While the overshoot does not change. This is because the actual i_{qLP} response behaves like a ramp signal instead of a step signal, hence the high frequency component in i_{qLP} response is much less than a step signal. The reduction of high frequency component helps reduce the overshoot. Therefore, by increasing the current-loop bandwidth for the BTB_L converter, i_{qBTBL} can track i_{qLP} faster without increasing overshoot.

From above it can be concluded that the current-loop bandwidth for the BTB_L converter should be selected

as large as possible. However, as revealed in [11], the current-loop bandwidth is physically restricted by the switching frequency f_{sw}. In our case, f_{sw}=16kHz, so the bandwidth should be smaller than 0.18×16kHz =2.8 kHz (Lang et al., 2019, [11]). Hence, the bandwidth is suggested to be larger than 1kHz but smaller than 2.8 kHz. As a trade-off, the current-loop bandwidth for the BTB_L converter is set as 1.5kHz.

3.2 Adaptive DC Voltage Control for the BTB Converter

As shown in Figure 9, there is a PI controller used to regulate the gain *m*. The PI parameters need to be carefully selected to ensure stability and control performance. The modelling, control plant analysis, and control design are presented in the following.

Based on the assumption that the power losses on the BTB_L converter is negligible compared with the transferred power, the power balance between the AC input and the DC output of the $B2B_L$ converter can be expressed as shown in Equation (13):

$$1.5\left(v_{dBTBL}i_{dBTBL}+v_{qBTBL}i_{qBTBL}\right)=v_{BTB}i_{BTB} \tag{13}$$

where v_{BTB} and i_{BTB} are the DC voltage and DC current of the BTB converter, respectively. v_{dBTBL}, v_{qBTBL}, i_{dBTBL} and i_{qBTBL} are the *dq* axes voltages and currents of the BTB_L converter, respectively. The power relation in Equation (13) can be linearized as follows, where the overbar and Δ are the steady state operating point and the small deviation:

$$\frac{3}{2}\left[\begin{array}{l}\left(\overline{v}_{dBTBL}+\Delta v_{dBTBL}\right)\left(\overline{i}_{dBTBL}+\Delta i_{dBTBL}\right)+\\ \left(\overline{v}_{qBTBL}+\Delta v_{qBTBL}\right)\left(\overline{i}_{qBTBL}+\Delta i_{qBTBL}\right)\end{array}\right]=\left(\overline{v}_{BTB}+\Delta v_{BTB}\right)\left(\overline{i}_{BTB}+\Delta i_{BTB}\right) \tag{14}$$

In the steady state, the following relations can be derived given that the LP generator operates without field-weakening:

$$\begin{cases}1.5\left(\overline{v}_{dBTBL}\overline{i}_{dBTBL}+\overline{v}_{qBTBL}\overline{i}_{qBTBL}\right)=\overline{v}_{BTB}\overline{i}_{BTB}\\ \Delta v_{dBTBL}\Delta i_{dBTBL}\approx 0 \quad \Delta v_{qBTBL}\Delta i_{qBTBL}\approx 0 \quad \Delta v_{BTB}\Delta i_{BTB}\approx 0\\ \overline{i}_{dBTBL}=m\cdot\overline{i}_{dLP}=0\end{cases} \tag{15}$$

Substituting Equation (15) into Equation (14) yields:

$$\frac{3}{2}\left[\overline{v}_{dBTBL}\Delta i_{dBTBL}+\overline{v}_{qBTBL}\Delta i_{qBTBL}+\overline{i}_{qBTBL}\Delta v_{qBTBL}\right]=\overline{v}_{BTB}\Delta i_{BTB}+\overline{i}_{BTB}\Delta v_{BTB} \tag{16}$$

The DC-link relation of the BTB_L converter can be expressed as shown in Equation (17):

$$C_{BTB}s\cdot\Delta v_{BTB}=\Delta i_{BTB}-\Delta i_{L\_BTB} \tag{17}$$

According to the control diagram shown in Figure 9, the following relation can be derived:

$$\begin{cases}\Delta m=\left(K_{pBTB}+\dfrac{K_{iBTB}}{s}\right)\left(\Delta v_{BTB}{}^{*}-\Delta v_{BTB}\right)\\ \Delta i_{dBTBL}=i_{dLP}\Delta m \qquad \Delta i_{qBTBL}=i_{qLP}\Delta m\end{cases} \tag{18}$$

where K_{pBTB} and K_{iBTB} are the v_{BTB} controller parameters.

The AC side electrical dynamics of the BTB_L converter can be described as follows in the *dq* frame:

$$\begin{cases} v_{dLP} = L_1 \dfrac{di_{dBTBL}}{dt} + v_{dBTBL} - \omega_{eLP} L_1 i_{qBTBL} \\ v_{qLP} = L_1 \dfrac{di_{qBTBL}}{dt} + v_{qBTBL} + \omega_{eLP} L_1 i_{dBTBL} \end{cases} \tag{19}$$

where L_1 is the equivalent inductance of the inductor L_1, v_{dLP} and v_{qLP} are the *dq* voltages of the LPG, respectively, and ω_{eLP} is the electrical speed of the LPG. Applying Equations (17)-(19) into Equation (16) gives:

$$\frac{3}{2}\left[\bar{i}_{qLP}\left(\bar{v}_{qBTBL} - \bar{i}_{qBTBL} L_1 \cdot s\right)\Delta m + \bar{i}_{qBTBL}\Delta v_{qLP}\right] = \left(\bar{v}_{BTB} C_{BTB} \cdot s + \bar{i}_{BTB}\right)\Delta v_{BTB} + \bar{v}_{BTB}\Delta i_L \tag{20}$$

Based on Equation (20), the block diagram of the BTB converter DC-link voltage control can be built as shown in Figure 11, where the derived control plant is outlined. T_d is the time constant of a first-order module which represents the time delay from sensing LPG's phase currents to taking the control actions for the BTB_L converter. T_d is typically regarded as 1.5×(PWM period) (Bozhko et al., 2017, [12]).

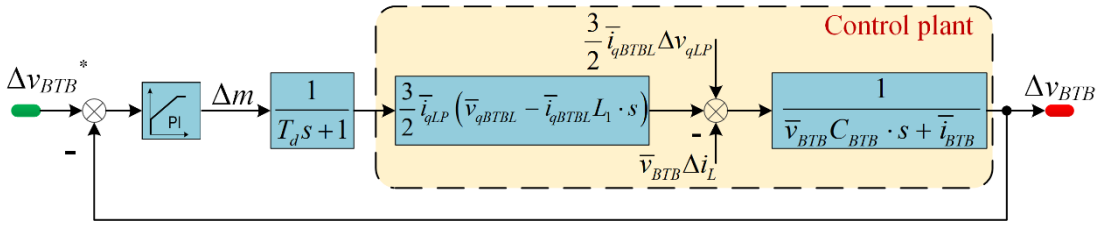

Figure 11. Block diagram of the BTB converter DC-link voltage control.

The zero provided by the v_{BTB} controller is used to cancel the dominant pole of forward path. Hence, the tuning criteria for control parameters can be derived as shown in Equation (21):

$$\begin{cases} K_{pBTB} = \alpha \cdot \bar{v}_{BTB} C_{BTB} \\ K_{iBTB} = \alpha \cdot \bar{i}_{BTB} \end{cases} \tag{21}$$

where α is a gain used to tune the control parameters.

As revealed in Section 2, the highest speed and heaviest load power is identified as the worst operating condition. Hence, based on the system parameters shown in Table 1and the worst operating point, the root locus of the BTB converter DC-link voltage control system with respect to the gain α is presented in Figure 12. It can be seen that when α = 0.05, the damping ratio is 0.707 and the overshoot is 4.25%. The closed-loop poles (-3150±3130i) are located at the left half plane, which ensures the stability. Hence, α = 0.05 is used for the following verifications.

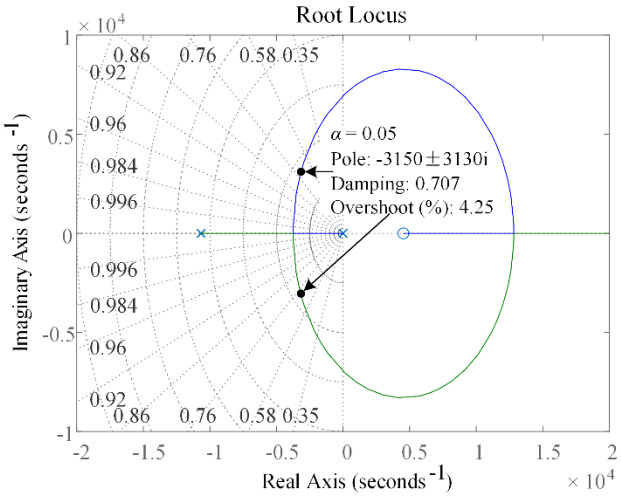

Figure 12. Root locus of the BTB converter DC-link voltage control system.

Table 1. System parameters of the AIPC.

Category	Parameter	Value
Electrcial machines	Full Speed of the LPG	4,000 rpm
	Full Speed of the HPG	15,000 rpm
	Base speed	8,000 rpm
	Stator inductance	0.1 mH
	Flux linkage of rotor	0.036 Wb
Main DC Bus	Rated voltage	270 V
	Main bus capacitor	1.2 mF
Back-to-back Converter	DC-link voltage	390 V
	DC-link capacitor	1.6 mF
	Switching frequency	16 kHz
	Current loop bandwidth	1.5 kHz
Other control paramters	Voltge loop gains for the rectifiers	Adaptively tuned, the gain γ = 0.4 in (8)
	Voltge loop gains for the BTB converter	Adaptively tuned, the gain α = 0.05 in (19)

4.0 EXPERIMENTAL VALIDATIONS

To test the performance of the proposed control schemes and engine performance improvement using EPT, an engine emulator and AIPC rig is built as shown in Figure 13. Two induction machines perform as prime movers, mimicking behaviour of the HP and LP shaft, respectively. Speed setpoints for the prime movers come from an engine model which is implemented in a dSpace. Two identical PMMs are used as HP and LP generators, whose parameters can be found in Table 1. Two identical rectifiers are used, so in the test the two droop gains are set identical. Functionalities include the main DC bus voltage and power sharing regulation, LP channel phase current synchronization, DC-link voltage control of the BTB converter, and engine performance improvement with EPT, will be illustrated in this section.

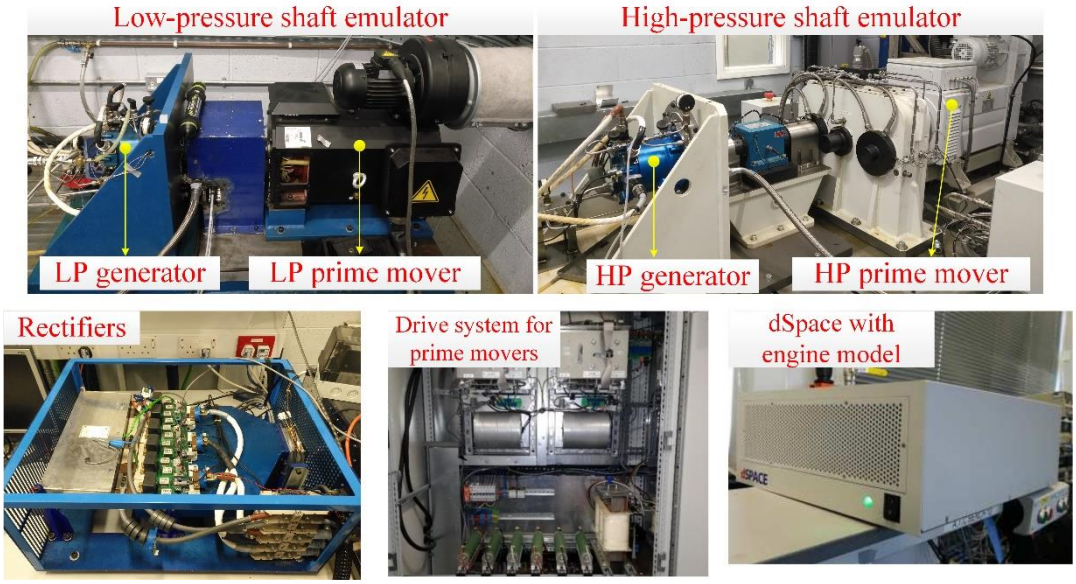

Figure 13. ***AIPC experimental setup.***

4.1 The Main DC Bus Voltage Control and Power Sharing

Control scheme for the rectifiers has been presented in Figure 8. Control performance of the main DC bus at various load power is exhibited in Figure 14, where the whole process is divided into five phases. In Phase 1 and 5, a constant power load (CPL) consumes 1.85kW power. In Phases 2 and 4, the CPL increases to 2.35kW. In Phase 3, the CPL consumes more power, resulting in a 3.1kW total load power.

The results of v_{dc}, i_{dcHP} and i_{dcLP} are presented in Figure 14. It can be seen that as the increase of load power, v_{dc} deviates from the rated value to 265V, 255V and 253V due to the droop control effect. i_{dcHP} is the same as i_{dcLP}, which means output power of the HP and LP rectifiers are controlled as identical. The results in Figure 14 show excellent main DC bus voltage control performance in both steady and transient states. Equivalent power sharing is also achieved using droop control.

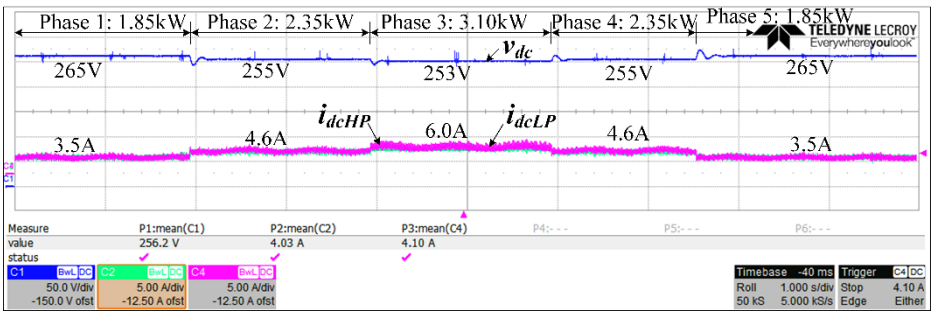

Figure 14. The DC voltage and currents at different load powers.

4.2 LP Channel Phase Current Synchronization and DC-link Voltage Control of the BTB Converter

To verify the effectiveness of the BTB converter control in Figure 9, results of the LP generator (LPG) phase current i_{aLP}, BTB_L converter phase current i_{aBTBL}, and the DC-link voltage of the BTB converter v_{BTB} are

shown in Figure 15. It can be seen that i_{aLP} and i_{aBTBL} are synchronized in phase. The peak value of i_{aLP} is 13.1A, that of i_{aBTBL} is 8.8A. Thus, according to the relation in Equation (12), ratio between power of the LP generator and transferred power through the BTB converter is 13.1/8.8=1.5. It means two third of LPG's power is transferred from the LP channel to the HP channel through the BTB converter, and one third of LPG's power is delivered to the main DC bus through the LP rectifier.

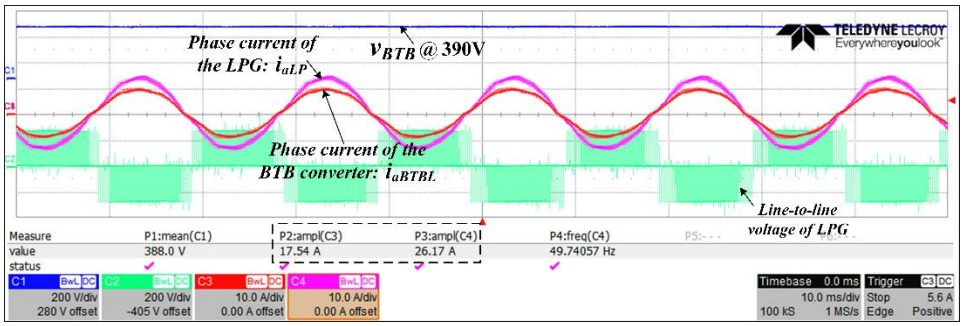

Figure 15. LP Cjannel Phase Current Synchronisation.

In Figure 15 one can also see that v_{BTB} is regulated to the designed value 390V. From the results, the proposed control scheme for the BTB converter shown in Figure 9 is verified.

4.3 Engine Performance with Electric Power Transfer

The BTB converter establishes an electrical path between the LP and HP electrical power channels. By transferring power from the LP to HP channel, and controlling the HPG in motoring mode, mechanical power can be extracted from the LP shaft of engine and transferred to the HP shaft. To study the engine performance with electric power transfer (EPT), a multi-spool turbofan model is developed using the intercomponent volume method and CFM56-3 engine generic maps (Enalou and Bozhko, 2020, [6]), (Enalou and Bozhko, 2021, [13]). One of achieved experimental result is given in Figure 16.

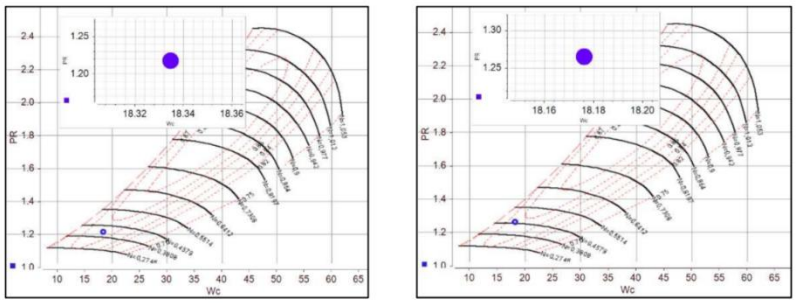

Figure 16. Compressor map of low-pressure compressor of engine at flight idle mode, 5kft, Mach=0.4.

At flight idle condition (5kft, Mach=0.4), the main controller is on HP speed. So, the HP speed is kept constant, and the LP speed decreases. 10kW power is transferred from the LP channel to HP channel electrically, and it is scaled into 200kW to feed the engine model in dSpace in real time. As can be observed in Figure 16, by transferring 200kW power from the LP shaft to the HP shaft of engine, the operating point of LP compressor moves to lower speed lines with lower pressure ratio. It is obvious that the compressor surge margin is enlarged as a result of the power transfer.

5.0 CONCLUSION

An advanced integrated power centre for MEA application is proposed in this study, based power electronic controlled PMM generators that off-take power from a jet engine shafts (LP and HP). The main benefit of the proposed centre is a decoupling of engine shafts thermodynamics that is achieved by electrical power transfer. Theoretical analysis shows great benefits of this concept in achieving enhancements in both engine and electrical side performances. The control design for the proposed power electronic based system is reported. The paper also reports experimental results that have demonstrated the concept, validating the control performance and engine performance enhancement by implementing the electric power transfer between engine spools.

REFERENCES

[1] Wheeler, P. W., Clare, J. C., Trentin, A. & Bozhko, S. 2013. An overview of the more electrical aircraft. Proceedings of the Institution of Mechanical Engineers, Part G: Journal of Aerospace Engineering, 227, 578-585.

[2] Enalou, H. B., Lang, X., Rashed, M. & Bozhko, S. 2020. Time-Scaled Emulation of Electric Power Transfer in the More Electric Engine. *IEEE Transactions on Transportation Electrification,* 6**,** 1679-1694.

[3] Gao, F. & Bozhko, S. 2016. Modeling and impedance analysis of a single dc bus-based multiple-source multiple-load electrical power system. IEEE Transactions on Transportation Electrification, 2, 335-346.

[4] Jia, Y. & Rajashekara, K. 2017. An Induction Generator-Based AC/DC Hybrid Electric Power Generation System for More Electric Aircraft. IEEE Transactions on Industry Applications, 53, 2485-2494.

[5] Lang, X., Yang, T., Li, C., Enalou, H. B., Bozhko, S. & Wheeler, P. 2020. A Dual-Channel-Enhanced Power Generation Architecture with Back-to-Back Converter for MEA Application. IEEE Transactions on Industry Applications, 56, 3006-3019.

[6] Enalou, H. B. & Bozhko, S. 2020. Performance improvement of turbofans by electric power transfer. Journal of Turbomachinery, 142.

[7] Li, C., Yang, T., Kulsangcharoen, P., Lo Calzo, G., Bozhko, S., Gerada, C. & Wheeler, P. 2019. A Modified Neutral Point Balancing Space Vector Modulation for Three-Level Neutral Point Clamped Converters in High-Speed Drives. IEEE Transactions on Industrial Electronics, 66, 910-921.

[8] Gao, F., Bozhko, S., Asher, G., Wheeler, P. & Patel, C. 2016. An Improved Voltage Compensation Approach in a Droop-Controlled DC Power System for the More Electric Aircraft. IEEE Transactions on Power Electronics, 31, 7369-7383

[9] Jalili, K., & Bernet, S. 2009. Design of LCL Filters of Active-Front-End Two-Level Voltage-Source Converters. *IEEE Transactions on Indutrial Electronics,* 56, 1674-1689.

[10] X. Zhang, X., & Yang, J. 2017. A DC-Link Voltage Fast Control Strategy for High-Speed PMSM/G in Flywheel Energy Storage System. IEEE Transactions on Industrial Applications, 54, 1671-1679.

[11] Lang, X., Yang, T., Enalou, H. B., Bozhko, S. & Wheller, P. An Enhanced Power Generation Centre for More Electric Aircraft Applications. 2019.A. M. Diab *et al*., "Fast and Simple Tuning Rules of

Synchronous Reference Frame Proportional-Integral Current Controller," *IEEE Access*, vol. 9, pp. 22156-22170, 2021.

[12] Bozhko, S., Rashed, M., Hill, C. I., Yeoh, S. S. & Yang, T. 2017. Flux-Weakening Control of Electric Starter-Generator Based on Permanent-Magnet Machine. IEEE Transactions on Transportation Electrification, 3, 864-877..

[13] Balaghi Enalou, H. & Bozhko, S. 2021. Electric Power Transfer Concept for Enhanced Performance of the More Electric Engine. Journal of Engineering for Gas Turbines and Power.